Applied Catalysis B: Environmental 140–141 (2013) 483–492

Contents lists available at SciVerse ScienceDirect

Applied Catalysis B: Environmental

journal homepage: www.elsevier.com/locate/apcatb

Identification of the active sites on CeO_2–WO_3 catalysts for SCR of NO_x with NH_3: An *in situ* IR and Raman spectroscopy study

Yue Peng[a], Kezhi Li[a], Junhua Li[a,b,*]

[a] State Key Joint Laboratory of Environment Simulation and Pollution Control, School of Environment, Tsinghua University, Beijing 100084, China
[b] State Environmental Protection Key Laboratory of Sources and Control of Air Pollution Complex, Tsinghua University, Beijing 100084, China

ARTICLE INFO

Article history:
Received 16 February 2013
Received in revised form 15 April 2013
Accepted 16 April 2013
Available online 25 April 2013

Keywords:
$DeNO_x$
NH_3-SCR
CeO_2
$Ce_2(WO_4)_3$
In situ IR
Raman

ABSTRACT

A series of CeO_2–WO_3 (W_xCe) catalysts were prepared for the SCR of NO_x with NH_3. Among the three representative samples, the W_1Ce catalyst exhibited great activity during SCR reaction and a large amount of N_2 from NH_3 oxidation, whereas the $W_{0.05}Ce$ catalyst yielded more NO from NH_3 oxidation than the W_3Ce at high temperature. Three types of metal oxide species (isopolytungsten species, $Ce_2(WO_4)_3$ compounds and crystalline WO_3) were observed on the catalyst surfaces with increased WO_3 loading. CeO_2, rather than WO_3 or $Ce_2(WO_4)_3$, presented favorable reducibility behavior. Furthermore, CeO_2 with intrinsic oxygen vacancies and unsaturated W^{n+} cations of crystalline WO_3 provided Lewis acid sites; meanwhile, the W—O—W or W═O modes of $Ce_2(WO_4)_3$ provided Brønsted acid sites. Based on the Raman spectra, the W—O species of the [WO_4] or [WO_6] units could be the active sites. The results suggest a reaction mechanism consisting of two independent cycles, denoted as a redox cycle due to the excellent oxygen storage capability and reducibility of cubic fluorite CeO_2 (for NH_3 activation) and an acid site cycle, resulting from Brønsted acid sites formed on the W—O—W species of $Ce_2(WO_4)_3$ (for NH_3 adsorption). Surface nitrate species cannot be involved directly in SCR reaction with gaseous NH_3; additionally, the adsorbed NO_2 demonstrated activity over the W_1Ce catalyst at 200 °C.

1. Introduction

Nitrogen oxides (NO_x) are emitted from the automobile exhaust gas and industrial combustion of fossil fuels, and today, NO_x is considered as a serious air pollutant. The selective catalytic reduction (SCR) with NH_3 is an effective technique for the NO_x abatement from diesel exhaust or coal-fired power plants, and the most widely employed catalyst in the industry is V_2O_5–WO_3/TiO_2 with a temperature window of 300–400 °C [1,2]. Based on *in situ* IR spectra, the well-known mechanistic scheme is described as follows: the V_2O_5-based catalysts follow a double-separated catalytic cycle, in which the acid-sites cycle adsorbs NH_3 on V^{5+}—OH as Brønsted acid sites, while the redox cycle activates the adsorbed NH_3 on the V═O groups [3,4]. In the review by Bañares et al., the *in situ* Raman spectra of the supported V_2O_5 catalyst revealed that the polymerized surface vanadia species exhibited higher activity than the isolated species. Moreover, they proposed that NH_3 initially adsorbed on the acid sites and then reduced the adjacent vanadia species (V^{5+} to V^{3+}) to create a vacancy for NO adsorption [5]. Giakoumelou et al. extensively studied the structure-activity relationship of the V_2O_5/TiO_2 catalysts with different surface VO_x densities. By correlating the *in situ* Raman spectra with the TOF values, they suggested that a V—O—V bridge or pairs of adjacent V—O—Ti sites rather than V═O groups, could be the active vanadia center at high surface densities [6]. Consequently, the *in situ* spectroscopy techniques (IR and Raman spectra) are extremely powerful and complementary tools, and are able to provide fundamental information regarding the adsorbed molecules and the active sites of catalytic reactions [7–9].

Although the V_2O_5-based catalysts show excellent activities, nonetheless the toxicity, high SO_2 oxidation activity, and low N_2 selectivity of vanadia limits its use in industrial applications and civilian vehicles [10]. Therefore, many researchers have attempted to develop new catalysts either without or with low vanadia loading to avoid the defects above. As important catalyst supports, ceria and ceria-containing materials have been widely employed as catalysts or structural promoters of heterogeneous catalytic reactions because of their favorable reducibility and remarkable oxygen storage capability (OSC) [11]. Xu et al. found ceria significantly improved the SCR activity [12] and Gao et al. systematically studied the influence of Ce:Ti ratio on SCR performance utilizing CeO_2–TiO_2 catalysts prepared by the sol-gel method [13]. Mamede et al. synthesized WO_x/CeO_2 catalysts by co-precipitation and impregnation methods for hexane isomerization, and found that

* Corresponding author at: State Key Joint Laboratory of Environment Simulation and Pollution Control, School of Environment, Tsinghua University, Beijing 100084, China. Tel.: +86 10 62771093.
E-mail address: lijunhua@tsinghua.edu.cn (J. Li).

0926-3373/$ – see front matter © 2013 Elsevier B.V. All rights reserved.
http://dx.doi.org/10.1016/j.apcatb.2013.04.043

increasing the tungsten content enhanced the activity and selectivity to methylcyclopentane [14]. Joshi et al. studied the surface acidity of pure and tungsten-doped ceria by density functional theory (DFT) calculations. By employing the NH_3 molecule as a probe, their calculated results showed that both Lewis and Brønsted acid sites exhibited very weak behavior on pure ceria (1 1 1) surface. When incorporated with tungsten, Brønsted acid sites were improved significantly [15]. In our previous works, the prepared CeO_2–WO_3 or CeO_2–WO_3/TiO_2 catalysts yielded favorable SCR activity above 200 °C and broadened the activity window in comparison to the commercial catalysts; additionally, these catalysts also exhibited better resistance to SO_2 and alkali metals [16–20]. Shan et al. found that significantly high activity of $CeWO_x$ catalyst can be obtained from 250 to 450 °C even under a space velocity of 500,000 h^{-1}. They attributed this excellent NO conversion to the synergistic effect between Ce and W species. Furthermore, they correlated the activity with high dispersions of CeO_2 and WO_3 on the TiO_2 support, remarkable oxygen vacancies (O_v) on CeO_2, and large surface acidities [21,22].

However, some basic problems are still under debate, such as the essence of the synergistic effect, the detailed nature of the active sites, and direct evidence of the different impacts of Ce and W species for the SCR reaction. *In situ* Raman information of the non-vanadia-based catalysts under NH_3-SCR has seldom been reported. This work attempts to elucidate the role of Ce and W species on CeO_2–WO_3 catalysts during the SCR process by employing both *in situ* IR and Raman spectroscopy. A plausible reaction mechanism based on the results for the CeO_2–WO_3 catalysts is proposed.

2. Experimental methods

2.1. Catalyst preparation

The catalysts were prepared by a co-precipitation method. Appropriate amounts of cerium nitrate and ammonium paratungstate were dissolved in an oxalic acid solution, and excess urea solution was added with stirring, resulting in the precipitation of a solid. The precipitated solids were collected by filtration and then were washed with distilled water, followed by drying at 120 °C for 12 h and calcination at 500 °C for 5 h. Finally, the catalysts were crushed and sieved to 40–60 mesh. The samples, denoted as W_xCe, indicate the mass ratio of WO_3 on the catalysts.

2.2. SCR performance

Activity measurements were performed in a fixed-bed quartz reactor (inner diameter of 5 mm) using 100 mg of catalyst measuring 40–60 mesh. The feed gas mixture contained 500 ppm NO, 500 ppm NH_3, 3% O_2, and the balance gas was N_2. The total flow rate of the feed gas was 200 cm^3 min^{-1} and the gas hourly space velocity (GHSV) was approximately 120,000 h^{-1}. Here, to ensure the reaction order was zero with respect to the NH_3, the concentration of NH_3 was usually slightly higher (50 ppm) than that of NO. The concentrations of the gases (NO, NO_2, N_2O, and NH_3) were continually monitored by an FTIR spectrometer (MultiGas TM 2030 FTIR Continuous Gas Analyzer). The concentration data were collected when the reaction reached a steady state after 30 min at each temperature.

To better evaluate the catalytic activity, the kinetic parameters were calculated according to the following equation, applied to the NO conversion:

$$k = -\frac{V}{W} \times \ln(1 - x) \quad (1)$$

In the above equation, k is the reaction rate constant (cm^3 g^{-1} s^{-1}), V is the total gas flow rate (cm^3 s^{-1}), W is the mass of catalyst in the reactor, and x is the NO conversion in the testing activity. The equation is based on the understanding that the reaction is first order dependent on NO and zero order dependent on NH_3 [2].

2.3. Catalyst characterization

Characterization of the BET surface area of the samples was carried out with a Micromeritics ASAP 2020 apparatus. The crystal structure was determined using X-ray diffraction (XRD) measurements (Rigaku, D/max-2200/PC) between 20° and 80° at a step rate of 10° min^{-1} operating at 40 kV and 30 mA using Cu Kα radiation. X-ray photoelectron spectroscopy (XPS) was performed with an ESCALab220i-XL electron spectrometer from VG Scientific using 300 W Al Kα radiations. The binding energies were referenced to the C 1s line at 284.8 eV. Temperature programmed reduction (TPR) experiments were performed on a chemisorption analyzer (Micromeritics, ChemiSorb 2720 TPx) under a 10% H_2/Ar gas flow (50 mL min^{-1}) at a rate of 10 °C min^{-1} up to 650 °C. Each sample was pretreated at 350 °C in He for 1 h before testing. The H_2 consumption of each catalyst preparation was calculated by comparison with that of a standard CuO sample.

2.4. In situ Raman spectroscopy

In situ Raman spectra were measured using a Raman microscope (InVia Reflex, Renishaw) equipped with a deep-depleted thermoelectrically cooled charge-coupled device (CCD) array detector and a high-grade Leica microscope (long working distance objective 50×). The sample was placed into the sample cell, which is specially designed for catalytic reactions carried out at high temperature and pressure (CCR 1000, Linkam fitted with quartz windows). The samples (25 mg) with particles larger than 60 mesh were mounted on nonreactive disposable ceramic fabric filters, placed inside the ceramic heating element, which is capable of heating samples from ambient up to 1000 °C. The 532 nm line (5 mW at sample) of the laser was used for recording the Raman spectra. The sample was pretreated in flowing N_2 at 350 °C for 1 h, and then was cooled down to room temperature and switched to N_2 purging. The gas used for the experiments was a mixture of 10% H_2/N_2, 500 ppm NH_3/N_2, 500 ppm NO/N_2 and 5% O_2/N_2 with a total flow rate of 50 cm^3 min^{-1}.

2.5. In situ IR spectroscopy

In situ IR spectra were recorded on a Fourier transform infrared spectrometer (FTIR, Nicolet 6700) equipped with a SMART collector and an MCT detector cooled by liquid N_2. Diffuse reflectance measurements were performed *in situ* in a high-temperature cell with a ZnSe window. The catalyst particles (larger than 60 mesh) were loaded in the Harrick IR cell and heated to 350 °C under N_2 at a total flow rate of 100 cm^3 min^{-1} for 1 h to remove any adsorbed impurities. The background spectrum was collected in a flowing N_2 atmosphere and was subtracted from each sample spectrum. The spectra were recorded by accumulating 32 scans at a resolution of 4 cm^{-1}. Here, to diminish the influence of absorbance for different samples, the absorbance intensity was set to 3.00 for every sample at 100 °C when collecting the background spectra.

3. Results and discussion

3.1. Reaction performance

By comparing the activity profiles (Fig. S1) and reaction rate constants (k) (Table 1) of the prepared catalysts at 200 °C under a GHSV of 120,000 h^{-1}, three samples were identified for the further

Table 1
Reaction rate constants (k) of the prepared catalysts at 200 °C.

	CeO_2	$W_{0.05}Ce$	$W_{0.2}Ce$	$W_{0.5}Ce$	W_1Ce	$W_{1.5}Ce$	W_3Ce
k ($cm^3\ g^{-1}\ s^{-1}$)	1.16	10.91	40.15	69.48	90.80	32.56	11.82
$100 \times k$ ($cm^3\ m^{-2}\ s^{-1}$)	1.46	9.68	–[a]	–	140.12	–	50.3

[a] Uncalculated.

study, including the $W_{0.05}Ce$, W_1Ce and W_3Ce with low, intermediate and high WO_3 loading, respectively. Fig. 1 presents the Arrhenius plots of the SCR reaction over the three catalysts. The W_1Ce exhibited a higher reaction rate than those of other catalysts. The absolute values of the slope of the fitting lines displayed the apparent activated barriers of the SCR reaction. W_1Ce showed the smallest energy barriers among the three catalysts. Additionally, the concentration of NO significantly increased in the higher temperature region for the pure CeO_2 and $W_{0.05}Ce$ catalysts (Fig. S1) due to the oxidation of NH_3 occurring in parallel with the SCR reaction.

Fig. 2 shows the specific transient experiments on the $W_{0.05}Ce$, W_1Ce and W_3Ce catalysts at 300 °C. When NO and O_2 were introduced, NO_2 from the NO oxidation was detected, and the concentrations of NO_2 decreased with increasing WO_3 loading. At the same time, less than 10 ppm N_2O (not shown in the figure) was observed and unchanged even with the introduction of NH_3 (Note: the N_2O is primarily the result of an instrumental artifact; *i.e.*, nearly no N_2O is created on the catalysts at 300 °C). As soon as NH_3 was introduced to the gas flow, both NO and NO_2 were remarkably decreased. The concentrations of NO_x exhibited the same trend as that of NO_x conversions. After 40 min, the NH_3 concentration increased slightly (20 ppm for the $W_{0.05}Ce$ and 50 ppm for the W_1Ce and W_3Ce). To hold the SCR reaction zero-order to NH_3, we added 50 ppm more NH_3 concentrations than NO. Thus, the lower concentration of NH_3 for the $W_{0.05}Ce$ catalyst could be due to NH_3 oxidation at this temperature.

Furthermore, to obtain quantitative information about NH_3 oxidation at high temperature, transient experiments were performed at 400 °C and the results are shown in Fig. 3. The outlet NH_3 concentration without O_2 was less than the inlet concentrations (520 ppm). This is due to the NH_3 oxidation with surface adsorbed oxygen on ceria. When O_2 was injected to the gas flow, the NH_3 concentration on both the $W_{0.05}Ce$ and W_1Ce decreased to about 100 ppm, however, the products of oxidation were N_2 and NO for the $W_{0.05}Ce$ catalyst and N_2 for the W_1Ce catalyst, respectively. These results suggest that the oxidation of NH_3 to NO occurs mainly on the ceria surface.

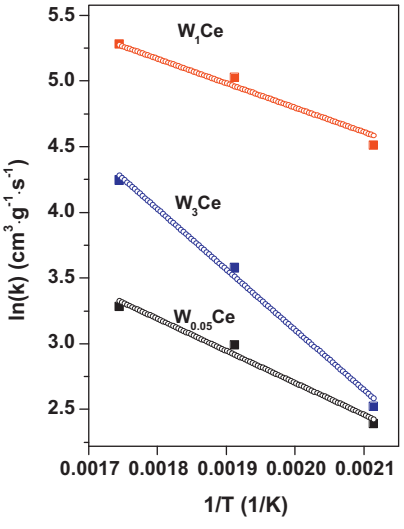

Fig. 1. (a) The Arrhenius plot for SCR performance over the $W_{0.05}Ce$, W_1Ce and W_3Ce (NO = NH_3 = 500 ppm, O_2 = 3%, balance N_2 with GHSV of 120,000 h^{-1}).

3.2. Structure characterization

An overview of basic characteristics of the prepared catalysts is summarized in Table 2. Small contents of WO_3 promoted the surface area of the catalyst; however, a reduction in surface area occurred on the W_1Ce and W_3Ce catalysts, due to the deposition of tungsten species on the ceria surface. The surface atomic ratio of W:Ce for the $W_{0.05}Ce$ presented a slightly higher value than theoretical ratio (0.04), indicating that tungsten prefers to bond on the ceria surface rather than in the bulk. The W_1Ce displayed a similar phenomenon, but for the W_3Ce catalyst, the ratio of W to Ce was found to be under the theoretical value (2.38), resulting from the formation of abundant bulk crystalline WO_3 or some new W-rich species.

The XRD patterns of the catalysts are shown in Fig. 4(a). All peaks can be assigned to the cubic fluorite phase of CeO_2 (PDF# 34-0394). With the increase of WO_3 loading, the diffraction peaks were broadened, accompanied by a decrease in their intensities. This can be attributed to a transformation of the bulk, regular crystals to an amorphous structure. The WO_3 phase in the catalysts cannot be directly determined through XRD analysis. It is likely that some of the tungsten atoms are incorporated into the cubic matrices of ceria (surface or subsurface) to form $W_xCe_{1-x}O_{2-\delta}$ solid solutions with a short-range order; alternatively, the WO_3 species could be highly dispersed on the surface of ceria. Chen et al. suggested that the WO_3 species could penetrate into the lattice structure of CeO_2, resulting in a replacement of Ce^{4+} by W^{6+} cations, leading to a corresponding decrease in the surface area [20]. Shan et al. proposed that the active sites of $CeWO_x$ catalysts were mainly CeO_2 with nanocrystalline and highly dispersed WO_3 [21]. Considering the ionic radii of Ce^{4+} (0.92 Å) and W^{6+} (0.62 Å), the replacement of Ce^{4+} by W^{6+} to form a solid solution is unexpected. A more likely explanation is that WO_3 moieties are directly bonded to the CeO_2 surface as amorphous structures by Ce—O—W linkages.

Normalized Raman spectroscopy (dehydrated) was employed to characterize the structure of the surface tungsten species (WO_x) on the ceria supports (Fig. 4(b)). The catalysts were first pretreated in N_2 at 350 °C for 1 h, and then the spectra were collected at room temperature (30 °C). Because of the high Raman scattering of the CeO_2 cubic phase in the $W_{0.05}Ce$, only 10% of the intensity contributed to its line. The spectra obtained for the $W_{0.05}Ce$ exhibited a peak at 464 cm^{-1}, which can be assigned to the characteristic F_{2g} mode of the symmetric breathing mode of oxygen atoms around cerium ions in the cubic phase CeO_2 (Ce—O). The peaks at 252 and 599 cm^{-1} can be assigned to a second-order transverse acoustic mode and a defect-induced mode, respectively [23–25]. When magnified over the region of 800–1000 cm^{-1}, several weak peaks due to the WO_x species can be observed. The peaks at 884 and 987 cm^{-1} can be attributed to the ν_{as} mode of W – O and the ν_s mode of W=O vibration of isopolytungstate species, respectively; the broad peak centered at approximately 810 cm^{-1} was likely due to the microcrystalline WO_3 [9,14]. The peak at 991 cm^{-1} required further attention because it could be another stretching mode of W=O. Theoretically, the tungsten atom could connect with two

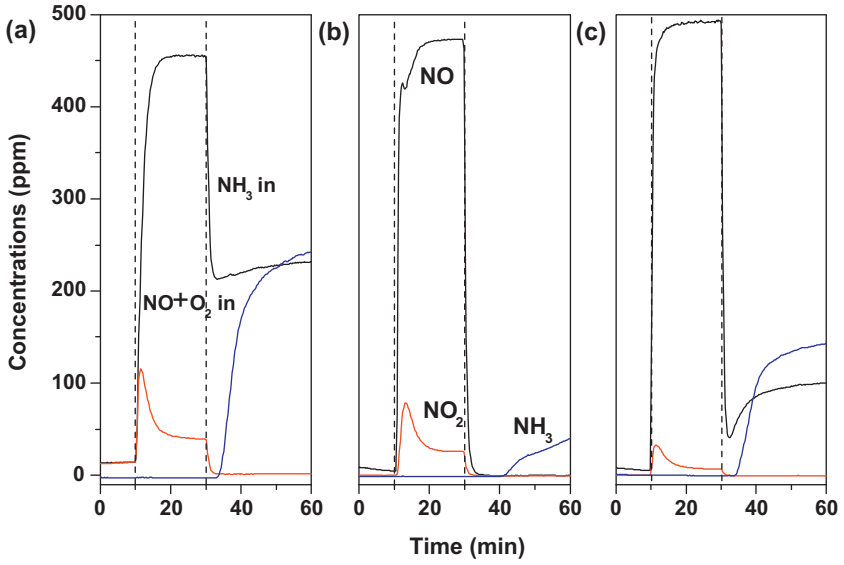

Fig. 2. Transient reaction under SCR gas flow over the (a) W0.05Ce, (b) W1Ce and (c) W3Ce at 300 °C.

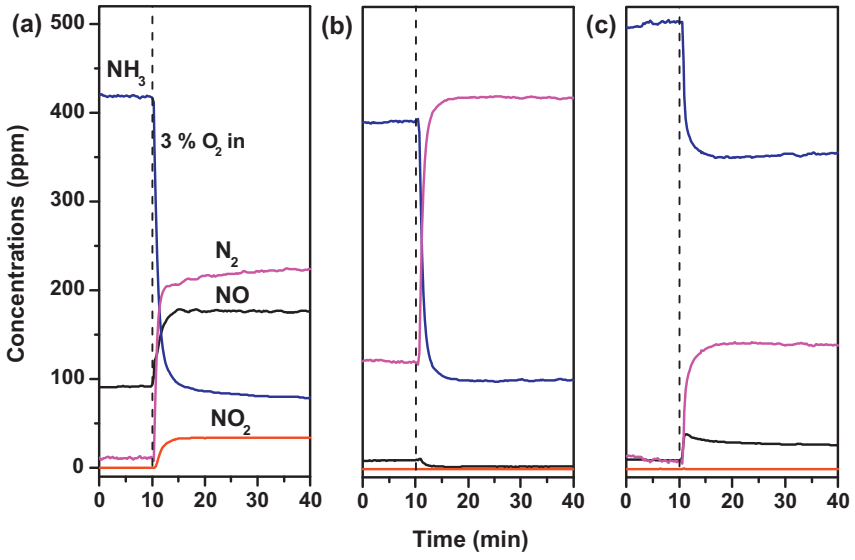

Fig. 3. Transient experiments with step feed of O_2 (3%) in NH_3 (520 ppm) over the (a) $W_{0.05}Ce$, (b) W_1Ce and (c) W_3Ce at 400 °C.

oxygen atoms by double bonds (a dioxo structure), creating a dioxo species with two bands, which would be visible in the Raman spectra with wavenumbers separated by approximately 20 cm^{-1} [5,26]. This phenomenon also can be observed in the spectra from the W_1Ce catalyst (925 and 940 cm^{-1}). For the W_1Ce catalyst, the F_{2g} mode of CeO_2 was decreased, while the peaks at 900–1000 cm^{-1} were significantly increased, which is in accordance with the XRD pattern results, indicating a low degree of crystallization on the W_1Ce catalyst. Moreover, the Ce—O vibration peak moved to a lower wavenumber from 464 to 460 cm^{-1}, in comparison to that of the $W_{0.05}Ce$ catalyst. This might be due to a decrease in the CeO_2 grain size [24]. In addition to the remarkably crystalline WO_3 species (270, 729 and 792 cm^{-1}) on the surface [14], several new peaks (340, 392, 817, 835, 896, 924 and 940 cm^{-1}) due to the $Ce_2(WO_4)_3$ compounds [14] were predominantly observed on the W_1Ce catalyst. When excess WO_3 was dispersed on the ceria

Table 2
The BET surface area (S_{BET}) values, the atomic ratios and the H_2 consumption by H_2-TPR of the prepared catalysts.

	S_{BET} ($m^2\ g^{-1}$)	Surface W: Ce[a]	H_2 con[b] (μmol g_{cat}^{-1})	H_2 con./surf.[c] (μmol m_{cat}^{-2})
CeO_2	79.2	–	375	4.74
$W_{0.05}Ce$	112.7	0.09	582	5.16
W_1Ce	64.8	1.11	1175	18.13
W_3Ce	23.5	1.75	615	26.17

[a] Calculated by the XPS results.
[b] H_2 consumption was calculated by the peak area of H_2-TPR.
[c] H_2 consumption per surface area was calculated by dividing the H_2 consumption into the corresponding BET surface area.

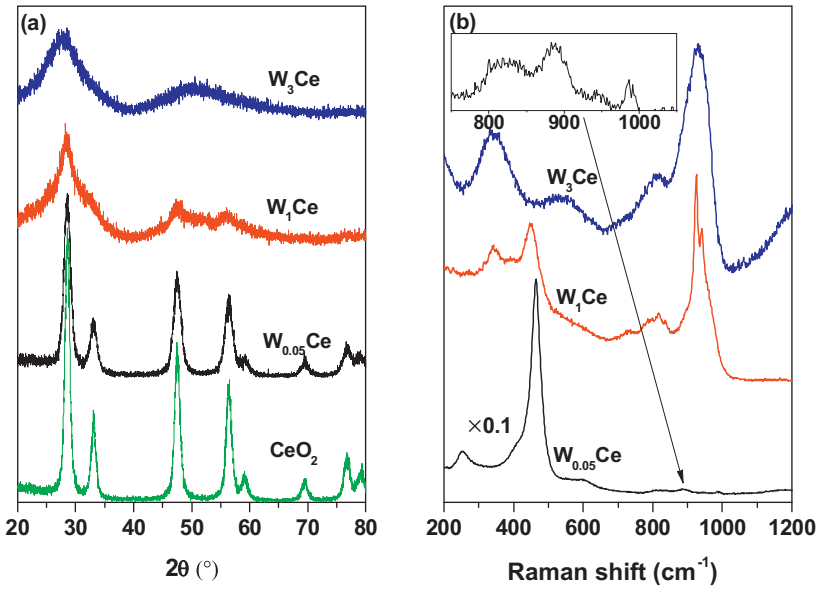

Fig. 4. (a) XRD patterns and (b) Raman spectra (dehydrated) of the $W_{0.05}Ce$, W_1Ce and W_3Ce and CeO_2.

(*i.e.*, the W_3Ce catalyst), the Ce—O mode was nearly undetectable, possibly as a result of overlapping fluorescence. The peaks assigned to the $Ce_2(WO_4)_3$ species were more apparent than in the spectra of the W_1Ce catalyst, and the dioxo structure of W=O bonds became indistinguishable, where only the peak at 929 cm^{-1} was detected. This suggests that the crystalline WO_3 and $Ce_2(WO_4)_3$ species, rather than the isopolytungstate species, are bonded to the ceria surface in the W_1Ce and W_3Ce catalysts.

The results indicate that all catalysts maintain the cubic fluorite phase of CeO_2. With the enhancement of the WO_3 amounts, the crystallization and surface area are decreased. At low WO_3 content, the surface WO_x species are an isopolytungstate coupled with microcrystalline WO_3; at intermediate and high WO_3 content, both crystalline WO_3 and $Ce_2(WO_4)_3$ are obtained and are the dominant surface species.

3.3. Redox properties

Fig. 5(a) shows the H_2-TPR profiles of the three catalysts and pure CeO_2 in the temperature range of 250–650 °C. The onset consumption order was $CeO_2 \sim W_{0.05}Ce < W_1Ce < W_3Ce$, indicating that reducible surface oxygen was suppressed or covered by increasing concentrations of WO_3. This can be due to the high thermal stability of the WO_3. The peak at 504 °C of pure CeO_2 could be attributed to the surface reduction of cerium atoms [26,27], and the corresponding H_2 consumption amount was 375 μmol g_{cat}^{-1}. When the tungsten was doped on ceria, the peak location moved to high temperature, and increasing WO_3 loading was found to lead to higher peak positions, indicating less facile reduction. However, the H_2 consumption amounts were significantly increased by the tungsten doping; especially when the surface areas of the samples were considered (Table 2). The increased H_2 consumption amounts could be responsible for not only the reduction of CeO_2 but the reduction of WO_3.

XPS spectra were employed to further characterize the surfaces. The spectra of O 1s for the three catalysts were investigated and the results are shown in Fig. 5(b). The O 1s peaks can be fitted into two peaks, referred to as the lattice oxygen at 529.3–530.3 eV (O_β) and the chemisorbed surface oxygen at 530.9–531.9 eV (O_α) [28]. As known, O_α is highly active in oxidation reactions due to its higher mobility than the lattice oxygen O_β. The fractions of O_α were

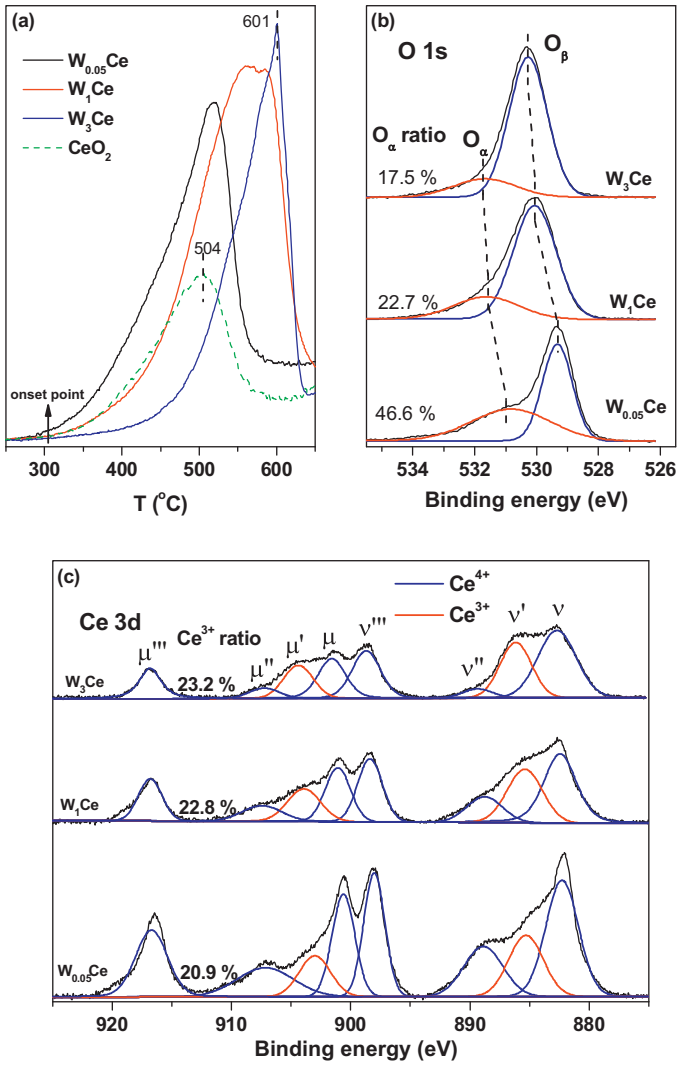

Fig. 5. (a) H_2-TPR profiles and XPS spectra of (b) O 1s and (c) Ce 3d of the $W_{0.05}Ce$, W_1Ce and W_3Ce and CeO_2.

46.6%, 22.7% and 17.5% for the $W_{0.05}Ce$, W_1Ce and W_3Ce catalysts, respectively, suggesting that surface active oxygen species in ceria can be covered by WO_3. Further, the binding energy of O_β moved to a high region at approximately 0.6 eV for the W_1Ce and 0.9 eV for the W_3Ce catalysts compared to the $W_{0.05}Ce$ catalyst, indicating that surface oxygen atoms could bond to some cations (W^{6+}) with higher oxidation states than that of Ce^{4+} [20]. The XPS spectra of W 4f were also obtained, and no significant change in the peak positions of the three catalysts (Fig. S2) was observed, suggesting that the chemical environment of the W^{6+} cations remained approximately the same. However, the peak intensities were enhanced with increasing WO_3 content on the ceria. The XPS spectra of Ce 3d for all three catalysts are shown in Fig. 5(c). The bands labeled μ, μ'', μ''', ν, ν'' and ν''' represented the $3d^{10}4f^0$ state of Ce^{4+}, whereas μ' and ν' represented the $3d^{10}4f^1$ state, corresponding to Ce^{3+} [29]. The fractions of Ce^{3+} cations are also calculated, and the results presented an opposite trend to that exhibited by O_α: according to this analysis, the Ce^{3+} cations were slightly increased by the WO_3 loading. Considering the trend of O_α fractions and the WO_x species on the ceria surfaces (Raman spectra), we assume that the Ce^{3+} cations originated from two sources: the intrinsic O_v of reduced CeO_2 and the $Ce_2(WO_4)_3$ compounds (Ce III). The reduction in O_α results in a reduction of the former, but the Ce III species from $Ce_2(WO_4)_3$ are significantly increased with WO_3 doping. Consequently, a net increase of Ce^{3+} cations occurs.

However, *in situ* Raman spectra of the TPR experiments were carried out for the same conditions. As a result of the different ways in which the data were obtained from each of the two methods (the data were measured as gas was passed through the TCD for H_2-TPR, yet were measured *in situ* on the sample surface for Raman TPR), errors can still exist. The Raman spectra of the three catalysts in the TPR experiments are shown in Fig. 6. For the $W_{0.05}Ce$, the peak intensities of the CeO_2 and highly dispersed WO_3 decreased with increasing temperature from 250 °C to 550 °C., The isopolytungstate species are undetectable at 500 °C, and only a weak peak at 459 cm^{-1} can be observed. The results show a good agreement with the H_2-TPR profiles. The Raman TPR profiles of the W_1Ce are displayed in Fig. 6(b). The F_{2g} mode was still apparent at 500 °C and then weakened at 550 °C and above. The results indicate that doping with tungsten could result in a low reducibility of ceria. For WO_x,

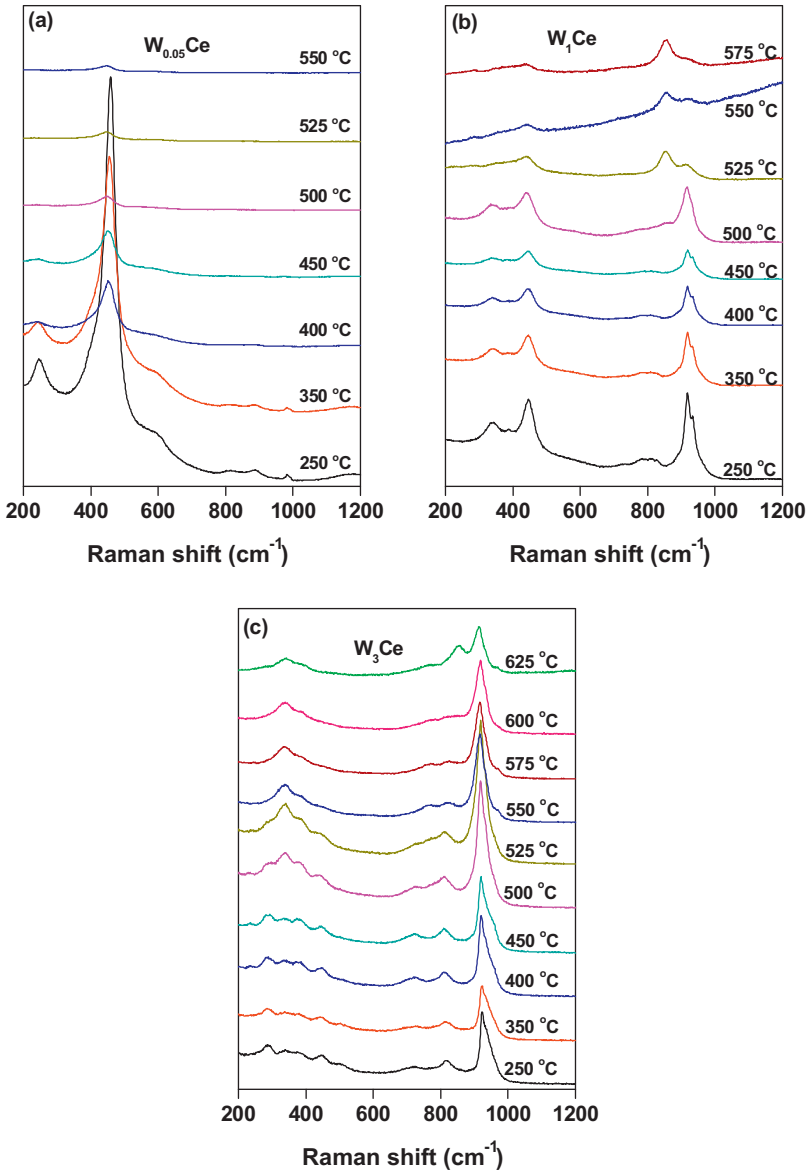

Fig. 6. *In situ* Raman spectra of the (a) $W_{0.05}Ce$, (b) W_1Ce and (c) W_3Ce under H_2/N_2 flow with a temperature-programmed treatment, as performed in the H_2-TPR experiments.

the peak intensities of 917 and 933 cm^{-1} were decreased, especially above 500 °C, as soon as a new peak at 853 cm^{-1} emerged. Mamede et al. assigned the peak at 846 cm^{-1} to $Ce_2(WO_4)_3$ for WO_x/CeO_2 catalysts calcined at 900 °C [14]. Upender et al. assigned the peak at 858 cm^{-1} to the stretching vibrations of W—O—W in [WO_4] or [WO_6] units for the TeO_2–WO_3 glass system [30]. We tentatively attribute this peak to the [WO_4] or [WO_6] units (amorphous) based on the reaction of W=O with H_2 at high temperature because this peak occurs as soon as the W=O vibrations (917 cm^{-1}) weakened. A similar phenomenon also can be obtained from the reduction of the W_3Ce catalyst (Fig. 6(c)) and the SCR reaction (Fig. 9 (a)). The results suggest that the W=O bonds of $Ce_2(WO_4)_3$ can be reduced to amorphous tungsten species by H_2. For the W-rich catalyst (Fig. 6(c)), the W=O species (295, 923 cm^{-1}) were significantly reduced only at temperatures above 600 °C. The peak at 856 cm^{-1} increased once the peak at 923 cm^{-1} decreased.

In summary, the results of the XPS, TPR and *in situ* Raman analyses indicate that tungsten doped on ceria could lower the reducibility of catalysts, as a result of two reasons: 1. The W—O—Ce bond is formed due to the strong interactions between the tungsten species and the surface ceria. Wu et al. found the V—O—Ce bridging mode directly from the Raman spectra, and ascribed the low reducibility of catalysts to the anchoring VO_x species [31]; 2. The reduction temperatures of W=O bonds, *i.e.*, 525 °C for the W_1Ce catalyst and 625 °C for the W_3Ce catalyst, are higher than that of Ce^{4+} to Ce^{3+}. The excellent reducibility during the SCR process can thus be attributed to the fluorite cubic CeO_2 rather than WO_3 or $Ce_2(WO_4)_3$.

3.4. Surface acidities

It has been established that the catalyst surface acidity plays an important role in the SCR reaction and that it is one of the most critical steps is the NH_3 adsorption. First, NH_3-TPD was employed to compare the acidities of the W_1Ce to pure CeO_2 and WO_3 catalysts (Fig. S3). The results displayed a significant increase in NH_3 adsorption over the W_1Ce catalyst. For pure CeO_2 or WO_3 oxides, however, the surface acidities were relatively weak. To explore the types, strengths and quantities of the surface acid sites in the catalysts, *in situ* IR spectrometry of NH_3 adsorption/desorption was employed. Fig. 7(a) shows the spectra of NH_3 species adsorbed on the $W_{0.05}Ce$, W_1Ce and W_3Ce catalysts at 100 °C, respectively. All spectra obtained at room temperature showed the presence of NH_3 adsorption bands at similar positions. The peaks centered at 1140 and 1564 cm^{-1} can be assigned to the ν_s and ν_{as} modes of the N—H bonds in NH_3 linked to Lewis acid sites, while the peaks at 1440 and 1668 cm^{-1} can be attributed to the ν_{as} and ν_s modes, respectively, of NH_4^+ chemisorbed on Brønsted acid sites [32,33].

The integrated peak area for peaks 1140 and 1440 cm^{-1}, representing the contributions of Lewis and Brønsted acid sites and their thermal stability over the three catalysts, is shown in Fig. 7(b), and the corresponding IR spectra of NH_3 desorption with temperature are shown in Fig. S4. The sequences are $W_1Ce \sim W_{0.05}Ce > W_3Ce$ for Lewis acidity and $W_1Ce \gg W_{0.05}Ce \sim W_3Ce$ for Brønsted acidity at 100 °C, and their quantities were found to decrease with increasing temperature up to 350 °C. Moreover, the stability of Lewis acidity of the W_1Ce catalyst was more significant than that of the $W_{0.05}Ce$ catalyst below 200 °C. The results indicate that CeO_2 mainly provides Lewis acid sites and that WO_x (with an appropriate doping amount) promotes the generation of Brønsted acid sites. Moreover, another type of Lewis acid site with relatively increased stability occurs on the surface due to the significant tungsten doping (W_1Ce). Considering the decrease in the surface coverage of cerium atoms and the O_α ratio by tungsten, it is possible that WO_x also could

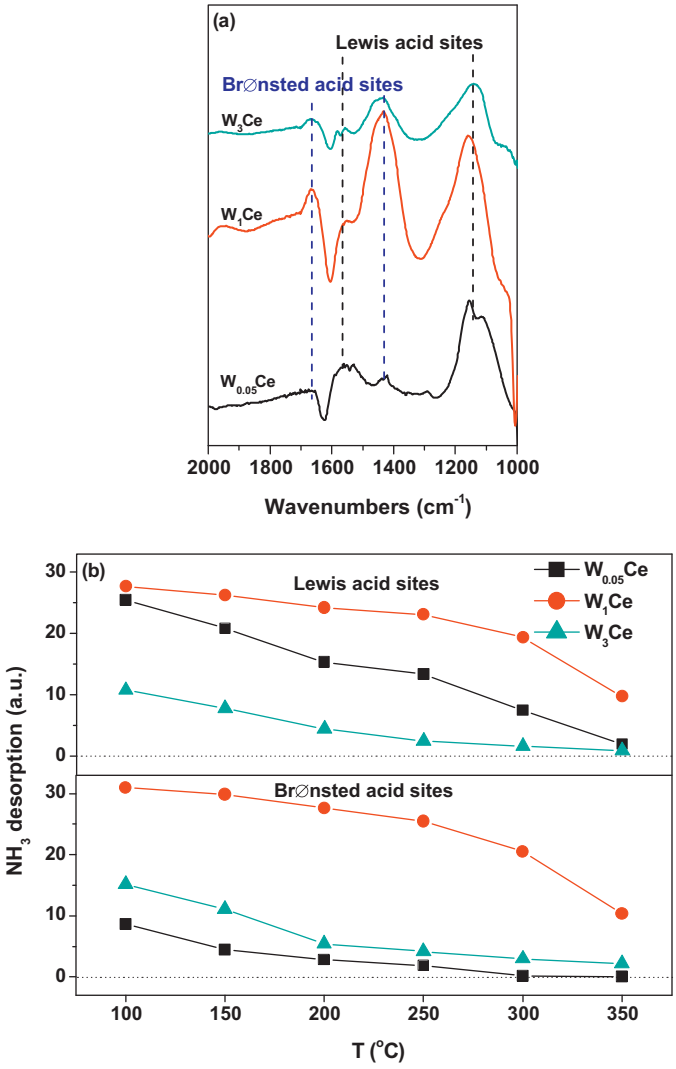

Fig. 7. (a) IR spectra of NH_3 adsorption at 100 °C and (b) the contributions of the Lewis and Brønsted acid sites over the $W_{0.05}Ce$, W_1Ce and W_3Ce.

present Lewis acid sites. Shan et al. reported similar results when studying the CeO_2–WO_3/TiO_2 catalyst, and they attributed their observations to the formation of unsaturated W^{n+} cations [22].

Joshi et al. proposed that the adsorption energies of NH_3 molecules bound to pure ceria at both Lewis and Brønsted acid sites were very weak. However, they ignored the influences of surface O_v on the ceria [15]. Nolan et al. extensively studied the electronic structures and molecular adsorptions on ceria with or without O_v by DFT + U calculations [34–36]. The O_v was associated with a reduction in two neighboring Ce^{4+} to Ce^{3+} in the cubic fluorite rather than partial reduction of all Ce ions, thereby producing several new unoccupied orbitals available to accept electrons from the lone pair orbitals of nitrogen in NH_3. Subsequently, this process led to the formation of Lewis acid sites. The XPS spectra of O 1s showed low O_α ratio with increased WO_3 loading, suggesting the minor formation of O_v on the catalyst surface. Further details concerning WO_x in the adsorption of NH_3 are shown and discussed below (Fig. 9).

3.5. Reaction details

The *in situ* IR spectra of reactive species adsorbed on the W_1Ce catalyst at 200 °C were measured, and the results are shown in Fig. 8. The catalyst was first pretreated with NH_3 for 1 h, followed by purging with N_2 to remove weakly bonded NH_3 (Fig. 8(a)).

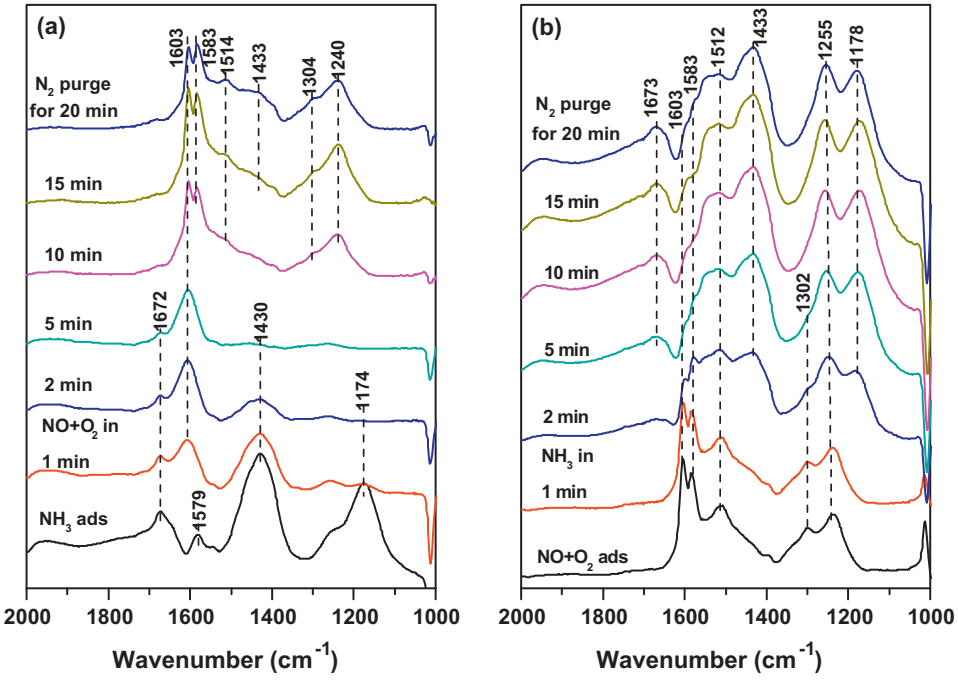

Fig. 8. *In situ* sequential IR spectra of the W_1Ce recorded at 200 °C under various atmospheres: (a) the dehydrated catalyst was first treated by NH_3, then NO + O_2 was added, and finally the NO + O_2 was stopped and (b) a reversed order of the gasses indicated was applied.

The peaks attributed to Lewis (1174 and 1579 cm^{-1}) and Brønsted (1430 and 1672 cm^{-1}) acid sites can be observed. After NO and O_2 were introduced to the IR cell, Lewis acidity decreased quickly, and Brønsted acidity diminished within 5 min, indicating that both Lewis and Brønsted acidities are reactive at 200 °C. Simultaneously, the peak at 1603 cm^{-1} was significantly increased, while other peaks at 1583, 1514, 1240 cm^{-1} as well as a shoulder centered at 1304 cm^{-1} were obtained after 5 min. The peak at 1603 cm^{-1} can be assigned to adsorbed NO_2; the peaks at 1583 and 1240 cm^{-1} can be assigned to bridging nitrate; and the peaks at 1514 and 1304 cm^{-1} can be assigned to bidentate nitrate [32]. Fig. 8(b) shows the *in situ* IR spectra in reversed order for detection of the reactive adsorbed NO_x species. First, the nitrate and adsorbed NO_2 species can be observed on the catalyst by purging NO and O_2 for 1 h. When NH_3 was introduced, the peak at 1603 cm^{-1} gradually decreased, but the other peaks attributed to nitrate species remained. The results suggest that nitrate species prefer to cover the catalyst surface rather than to react with gaseous or adsorbed

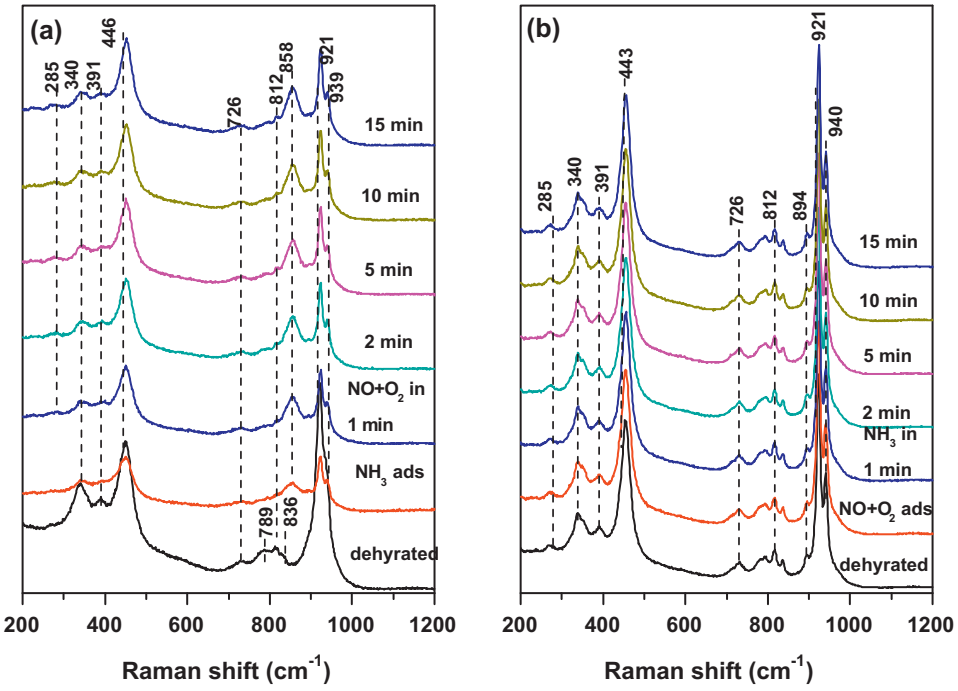

Fig. 9. *In situ* sequential Raman spectra of the W_1Ce recorded at 200 °C under various atmospheres: (a) the dehydrated catalyst was first treated by NH_3, then NO + O_2 was added, and finally the NO + O_2 was stopped and (b) a reversed order of the gasses indicated was applied.

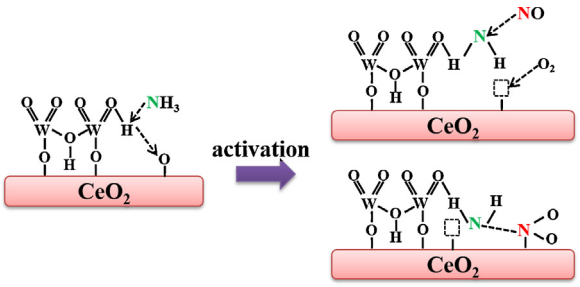

Fig. 10. Schematic of the plausible mechanism for NH_3 activation and oxidation on the CeO_2–WO_3 catalyst.

NH_3 species at 200 °C. After 5 min, the NH_3 species can be observed, indicating that most of the adsorbed NO_2 species have already been exhausted.

To further study the surface active sites during the adsorption and reaction processes, *in situ* Raman spectra were collected at 200 °C under similar conditions as during the IR spectra. After recording the spectra in N_2 atmosphere, an NH_3/N_2 stream was mixed and introduced to the Raman cell for 1 h (Fig. 9(a)). Both the crystalline WO_3 and $Ce_2(WO_4)_3$ species weakened, indicating that NH_3 is selectively chemisorbed on the surface of WO_x at 200 °C. The Ce—O vibration first declined by weak bonding of NH_3 on Lewis acid sites and then was enhanced after 1 min as a result of exposure to NO and O_2. Compared to the results of *in situ* IR spectra, we tentatively assign the weak Lewis acid sites to CeO_2, particularly to the contribution of the Ce^{3+} cations originating from the intrinsic O_v. We assign the strong Lewis acid sites to the unsaturated coordination of W^{n+} cations (crystalline WO_3) and the Brønsted acid sites to the hydroxy formed on the W—O—W or W=O modes of $Ce_2(WO_4)_3$. Further, the peak at 858 cm^{-1} is due to the W—O—W vibration in $[WO_4]$ or $[WO_6]$ units, which appeared and increased when NO and O_2 were introduced. The results indicate that either the $[WO_4]$ or $[WO_6]$ units are active during reaction between the adsorbed NH_x species and the gaseous NO_x species. To define the active species during the SCR reaction, another series of *in situ* sequential Raman spectra of the W_1Ce catalyst at 200 °C were also employed, and the results present the same species under the reaction gas flow (Fig. S5). That is, as soon as the intensities of the W=O vibrations decreased, the peak at approximately 858 cm^{-1} (857 or 854 cm^{-1}) appeared and increased in intensity. When the order of gas treatment was reversed (Fig. 9(b)), no discernible difference was observed between the Raman spectra. This suggests that the reaction between the adsorbed nitrate species and the NH_x species is very weak or cannot take place at 200 °C.

3.6. Reaction mechanism

Based on the *in situ* studies of the SCR process over the W_1Ce at 200 °C, specific reaction mechanisms can be inferred (Fig. 10). The gaseous NH_3 likely bonds to CeO_2 (on Ce^{3+}) or crystalline WO_3 (on W^{n+}) as Lewis acid sites and strongly bonds to $Ce_2(WO_4)_3$ (on W—O—W or W=O) as Brønsted acid sites. The gaseous NO or weakly adsorbed NO_2 species can react with activated NH_x species. Though the Lewis acidity of the W_1Ce catalyst decreased quickly during exposure to NO and O_2 in the IR spectra (Fig. 8(a)), consumption of NH_3 on the Lewis acid sites cannot be the predominant reaction pathway during the SCR process, considering the low SCR activity and high NH_3 oxidation ability (at high temperature) of the pure CeO_2 and $W_{0.05}Ce$ catalysts.

Yuan et al. systematically investigated the mechanisms of SCR and NH_3 oxidation reactions using a V_2O_5 cluster model and DFT calculations. They suggested that Lewis acid sites in the SCR reaction played either a small or insignificant role due to the high reaction barrier (51.3 kcal mol^{-1}) and the incorrect reaction order (independent of NO); whereas Brønsted acid sites stabilized NH_3 but are less significant with respect to the activation of NH_3 [37,38]. Previous studies also proposed that the TiO_2 anatase support exhibited only Lewis acidity with no SCR activity, while the vanadyl sites (Lewis acidity) can convert into Brønsted acid sites as a result of water adsorption [2]. Considering the similarity of properties between CeO_2 cubic fluorite and TiO_2 anatase (*i.e.*, surface acidity and O_v) [11,13], we suggest that the change from Lewis to Brønsted acid sites is possible and Lewis acidity alone cannot be the main active centers in the SCR reaction.

As the NH_3 interacts with surface $Ce_2(WO_4)_3$, it can change the W=O to W—O, forming $[WO_4]$ or $[WO_6]$ units, and bonding to these units as a result of Brønsted acidity, thereby becoming a more active intermediate species through the neighboring oxygen atom bonded to cerium (owing to the good OSC and reducibility of CeO_2). Then the NH_x ($x < 3$) species can react with NO to produce N_2 and H_2O, and the reduced Ce^{3+} cation can be returned to its original state, fulfilling the SCR cycle.

Moreover, the *in situ* sequential IR spectra of the W_1Ce catalyst at 150 °C and 300 °C under various atmospheres were also obtained (Figs. S6 and S7), with the reaction mechanisms showing similar results as those processed at 200 °C. Therefore, the SCR reaction mechanism discussed above with respect to the CeO_2—WO_3 catalyst can also be divided into the acid cycle, mainly from the contribution of appropriate Brønsted acidity over $Ce_2(WO_4)_3$, and the redox cycle, which is largely the result of the contributions of good OSC and reducibility provided by the CeO_2 cubic fluorite structure.

4. Conclusions

In situ IR and Raman spectroscopy coupled with TPR and XPS techniques were employed to investigate the surface adsorbed species and active sites during the SCR reaction of NO with NH_3 on W_xCe catalysts. The W_1Ce catalyst was found to yield better SCR performance, while the $W_{0.05}Ce$ catalyst exhibited preference for the oxidation of NH_3 to NO at high temperatures. Three species (isopolytungstate species, crystalline WO_3 and $Ce_2(WO_4)_3$) formed on the surface of the catalysts in accordance with the WO_3 loading, and the reducibility of the catalysts decreased when W—O—W, W=O and Ce—O—W bonds were formed. Lewis acid sites were originated from CeO_2 and some of the unsaturated W^{n+} cations of crystalline WO_3; additionally, Brønsted acid sites were formed on the W—O—W or W=O sites of $Ce_2(WO_4)_3$. The proposed reaction mechanism includes an acid site cycle (attributed mainly to the Brønsted acid site of $Ce_2(WO_4)_3$ (NH_3 adsorption) rather than to the weak Lewis acid sites), and a redox cycle (attributed to the good OSC and reducibility of cubic fluorite CeO_2 (NH_3 activation) rather than to $Ce_2(WO_4)_3$). The adsorbed nitrate species cannot directly react with gaseous NH_3; in contrast, only the adsorbed NO_2 species showed activity over the W_1Ce catalyst at 200 °C.

Acknowledgments

The authors gratefully acknowledge the National Natural Science Foundation of China (Grant No. 21221004) and the National High-Tech Research and Development Program of China (863) (Grant No. 2012AA062506) and the Science and Technology Department of Guangdong Province (Grant No. 2011A032303002).

Appendix A. Supplementary data

Supplementary data associated with this article can be found, in the online version, at http://dx.doi.org/10.1016/j.apcatb.2013.04.043.

References

[1] G. Ramis, F. Bregani, Applied Catalysis 64 (1990) 259–278.
[2] G. Busca, L. Lietti, G. Ramis, F. Berti, Applied Catalysis B: Environmental 18 (1998) 1–36.
[3] N. Topsoe, Science 265 (1994) 1217–1219.
[4] N. Topsoe, Journal of Catalysis 151 (1995) 226–240.
[5] M. Banares, I. Wachs, Journal of Raman Spectroscopy 33 (2002) 359–380.
[6] I. Giakoumelou, C. Fountzoula, C. Kordulis, S. Boghosian, Journal of Catalysis 239 (2006) 1–12.
[7] E. Stavitski, B. Weckhuysen, Chemical Society Reviews 39 (2010) 4615–4625.
[8] S. Alayoglu, J. Krier, W. Michalak, Z. Zhu, E. Gross, G. Somorjai, ACS Catalysis 2 (2012) 2250–2258.
[9] I. Wachs, C. Roberts, Chemical Society Reviews 39 (2010) 5002–5017.
[10] M. Amiridis, R. Duevel, I. Wachs, Applied Catalysis B: Environment 20 (1999) 111–122.
[11] M. Ganduglia-Pirovano, A. Hofmann, J. Sauer, Journal of Surface Science Report 62 (2007) 219–270.
[12] W. Xu, Y. Yu, C. Zhang, H. He, Catalysis Communications 9 (2008) 1453–1457.
[13] X. Gao, Y. Jiang, Y. Zhong, Z. Luo, K. Cen, Journal of Hazardous Materials 174 (2010) 734–739.
[14] A. Mamede, E. Payen, P. Grange, G. Poncelet, A. Ion, M. Alifanti, V. Pârvulescu, Journal of Catalysis 223 (2004) 1–12.
[15] A. Joshi, A. Rammohan, Y. Jiang, S. Ogunwumi, Journal of Molecular Structure 912 (2009) 73–81.
[16] L. Chen, J. Li, M. Ge, Environmental Science and Technology 44 (2010) 9590–9596.
[17] L. Chen, J. Li, M. Ge, L. Ma, H. Chang, Chinese Journal of Catalysis 32 (2011) 836–841.
[18] Y. Peng, J. Li, L. Chen, J. Chen, J. Han, H. Zhang, W. Han, Environmental Science and Technology 46 (2012) 2864–2869.
[19] Y. Peng, J. Li, W. Shi, J. Xu, J. Hao, Environmental Science and Technology 46 (2012) 12623–12629.
[20] L. Chen, J. Li, W. Ablikim, J. Wang, H. Chang, L. Ma, J. Xu, M. Ge, H. Arandiyan, Catalysis Letters 141 (2011) 1859–1864.
[21] W. Shan, F. Liu, H. He, X. Shi, C. Zhang, Chemical Communications 47 (2011) 8046–8048.
[22] W. Shan, F. Liu, H. He, X. Shi, C. Zhang, Applied Catalysis B: Environmental 115/116 (2012) 100–106.
[23] Z. Wu, M. Li, J. Howe, H. Meyer, S. Overbury, Langmuir 26 (2010) 16595–16606.
[24] J. Xu, P. Li, X. Song, C. He, J. Yu, Y. Han, Journal of Physical Chemistry Letters 1 (2010) 1648–1654.
[25] Z. Wu, M. Li, D. Mullins, S. Overbury, ACS Catalysis 2 (2012) 2224–2234.
[26] C. Bigey, L. Hilaire, G. Maire, Journal of Catalysis 198 (2001) 208–222.
[27] K. Zhou, X. Wang, X. Sun, Q. Peng, Y. Li, Journal of Catalysis 229 (2005) 206–212.
[28] F. Liu, H. He, Y. Ding, C. Zhang, Applied Catalysis B: Environmental 93 (2009) 194–204.
[29] A. Gupta, M. Hegde, K. Priolkar, U. Waghmare, P. Sarode, S. Emura, Chemistry of Materials 21 (2009) 5836–5847.
[30] G. Upender, V. Sathe, V. Mouli, Physica B 405 (2010) 1269–1273.
[31] Z. Wu, A. Rondinone, I. Ivanov, S. Overbury, Journal of Physical Chemistry C 115 (2011) 25368–25378.
[32] K. Hadjiivanov, Catalysis Reviews 42 (2000) 71–144.
[33] G. Qi, R. Yang, R. Chang, Applied Catalysis B: Environmental 51 (2004) 93–106.
[34] M. Nolan, S. Parker, G. Watson, Surface Science 595 (2005) 223–232.
[35] M. Nolan, S. Parker, G. Watson, Journal of Physical Chemistry B 110 (2006) 2256–2262.
[36] M. Nolan, Journal of Physical Chemistry C 113 (2009) 2425–2432.
[37] R. Yuan, G. Fu, X. Xu, H. Wan, Physical Chemistry Chemical Physics 13 (2011) 453–460.
[38] R. Yuan, G. Fu, X. Xu, H. Wan, Journal of Physical Chemistry C 115 (2011) 21218–21229.